


Article

Analytical Investigations of Nonlinear Stiffness Characteristics of Halbach-Cylinder Magnetic Springs for Heavy-Load Capacity

Zhongsheng Chen ^{1,2,*}, Yangyi Zhang ², Yeping Xiong ³  and Ankang Wang ²¹ School of Engineering Science, Shandong Xiehe University, Jinan 250107, China² College of Railway Transportation, Hunan University of Technology, Zhuzhou 412007, China; m23081100007@stu.hut.edu.cn (Y.Z.); m24081100027@stu.hut.edu.cn (A.W.)³ Faculty of Engineering and Physical Sciences, University of Southampton, Southampton SO16 7QF, UK; y.xiong@soton.ac.uk

* Correspondence: chenzhongsheng@sdxiehe.edu.cn

Abstract: Quasi-zero stiffness (QZS) has become a promising way of realizing low-frequency vibration isolation, where magnetic springs have been widely adopted for constructing negative stiffness. However, existing single-layer magnetic springs often have a small-amplitude negative stiffness, so the loading capacity is low. In order to address this issue, this paper presents novel Halbach-cylinder magnetic springs (HCMSs) by using the Halbach array. Firstly, stiffness formulas of basic single-layer magnetic springs are analytically built based on the Amperian current model. The stiffness of the HCMS is derived from combining multiple single-layer magnetic springs. Then, nonlinear stiffness characteristics of both single-layer magnetic springs and HCMSs are investigated in terms of the amplitude, the uniformity, and the displacement range of negative stiffness. Analytical results show that HCMSs can generate negative stiffness with different equilibrium positions, and the amplitude of negative stiffness of HCMSs is much larger than that of single-layer magnetic springs. The amplitude of negative stiffness is in conflict with the uniformity, so a trade-off design is needed. In addition, increasing the number of layers of Halbach cylinders can be adopted to realize larger-amplitude and wider-range negative stiffness. This study will provide new insights into designing QZS with heavy-load capacity.

Keywords: quasi-zero stiffness; heavy load; large-amplitude negative stiffness; magnetic spring; Halbach arrays; Halbach-cylinder magnetic spring



Academic Editor: Ephraim Suhir

Received: 16 February 2025

Revised: 1 May 2025

Accepted: 2 May 2025

Published: 3 May 2025

Citation: Chen, Z.; Zhang, Y.; Xiong, Y.; Wang, A. Analytical Investigations of Nonlinear Stiffness Characteristics of Halbach-Cylinder Magnetic Springs for Heavy-Load Capacity. *Appl. Sci.* **2025**, *15*, 5099. <https://doi.org/10.3390/app15095099>

Copyright: © 2025 by the authors. Licensee MDPI, Basel, Switzerland. This article is an open access article distributed under the terms and conditions of the Creative Commons Attribution (CC BY) license (<https://creativecommons.org/licenses/by/4.0/>).

1. Introduction

Vibration exists widely in nature, which is often defined as the mechanical movement of an object oscillating around an equilibrium position. However, vibration is undesirable in many domains, and unwanted vibrations can cause serious harm to mechanical systems, human health, and so on. For example, vibrations of vehicle seats often reduce ride comfort [1], vibrations of machine tools will reduce the manufacturing precision [2], and earthquake-induced vibrations will damage buildings [3]. In particular, mechanical vibrations are often a byproduct of mechanical systems, and it is impossible to eliminate vibration sources in practice. Vibration isolation can prevent vibration transmission between different components, so it is important to implement vibration isolators. Nowadays, linear isolators are always employed to reduce mechanical vibrations. According to the linear isolation theory, however, vibrations cannot be suppressed when the excitation frequency is less than $\sqrt{2}\omega_n$ (ω_n is the natural frequency of the mechanical system) [4]. This is a significant drawback of linear isolators since many systems require low-frequency vibration

isolation. One possible strategy for extending isolation ability to low-frequency bands is to reduce the stiffness of the system, but this approach will lead to low loading capacity and system instability. Therefore, innovative structures are needed to realize low-frequency or ultra-low-frequency vibration isolation.

In recent years, quasi-zero stiffness (QZS) vibration isolators have been proven to be an effective and feasible means to solve low-frequency vibration problems. The concept of QZS was first proposed by Alabuzhev [5] and is described as positive stiffness and negative stiffness. QZS has the unique feature of high static and low dynamic (HSLD) stiffness near the static equilibrium position, which can greatly reduce the dynamic stiffness without reducing the static stiffness. Therefore, QZS can be utilized to realize low-frequency vibration control and solve the contradiction between low natural frequency and small static deformation. In particular, the key point of QZS is to design proper negative-stiffness structures [6,7]. According to the literature, there are some ways of achieving negative stiffness. The first way is to use oblique springs. Carrella et al. [8] built a QZS-based vibration isolation system consisting of a vertical spring and two oblique springs in parallel. The second way is to use a spring and a rod. Liu et al. [9] proposed a QZS vibration isolator based on the 'spring-rod' structure. The third way is to use buckling beams. Liu et al. [10] built a large negative stiffness under small displacement by utilizing the Euler buckling beam. The fourth way is to use cams. Li et al. [11] built a QZS vibration isolator by using a cam structure whose profile was designed to follow the force-displacement relation of QZS. The fifth way is to use magnets. Chen et al. [12] used a pair of magnetic rings to generate QZS for low-frequency simultaneous vibration isolation and energy harvesting. To date, QZS has shown great potential in the field of low-frequency vibration isolation.

In recent years, the implementation of permanent magnets in QZS vibration isolators has attracted significant attention from many scholars. Among different kinds of negative-stiffness structures, the magnetic spring is commonly built by using a mobile magnet and a stationary magnet, which utilizes the repulsive or attractive forces between two permanent magnets to achieve negative stiffness. Zhu and Chai [13] gave a comprehensive review on magnetic negative stiffness in vibration isolation systems from theoretical models to engineering applications. Generally speaking, the shapes of magnetic springs can be rectangular [14] or circular [15] according to the shapes of the permanent magnets. For example, Akoun and Yonnet [16] proposed an analytical model to calculate the magnetic force between two three-dimensional rectangular permanent magnets based on the surface charge model. Zheng et al. [17] designed an HSLD stiffness isolator using a negative-stiffness magnetic spring, and the magnetic force between the inner and the outer magnets was then calculated based on the Amperian current model. Magnetic springs have the outstanding advantages of compact design, efficient space utilization, no mechanical friction, and fewer vibration transmission paths. In particular, the stiffness characteristics can be adjusted by varying the distance or orientation of the magnets. Therefore, magnetic spring-based QZS vibration isolators find promising vibration control applications across numerous fields [18,19]. More importantly, the loading capacity of a QZS vibration isolator strongly depends on the static positive stiffness. In most existing works, small payloads are always considered. However, there are still many heavy-load applications in practice, such as vehicle suspensions [20] and offshore platforms [21]. In these cases, a large-amplitude negative stiffness is always needed to match the large positive stiffness in order to generate the QZS. However, for existing single-layer magnetic rings, the negative stiffness near the equilibrium position is not always enough for heavy payloads. Therefore, it is very important to study novel magnetic structures with large-amplitude negative stiffness.

The Halbach array has been proposed to greatly increase the magnetic force in a limited space, which is a special arrangement of permanent magnets that enhances the

magnetic field on one side of the array [22,23]. In the literature, there are two main types of Halbach arrays, namely flat Halbach arrays [24,25] and Halbach cylinders [26]. In particular, Halbach cylinders are more suitable for compact design than flat Halbach arrays. The Halbach array offers a prior advantage over conventional layouts of magnets in terms of its concentrated magnetic-field intensity. Therefore, it is promising to introduce Halbach cylinders for designing novel magnetic springs. To the best of our knowledge, the application of Halbach arrays in QZS vibration isolators has not yet been reported. In particular, there are three key questions to be answered.

(1) Can single-layer magnetic springs definitely generate negative stiffness or not? Can Halbach array-based magnetic springs definitely generate large-amplitude negative stiffness or not?

(2) What kinds of Halbach array-based magnetic springs can generate large-amplitude negative stiffness? How can we select the optimal structural configuration?

(3) What are the effects of geometric parameters on negative stiffness metrics of Halbach array-based magnetic springs? How can we determine the geometric parameters?

To date, existing studies have seldom been carried out on Halbach array-based magnetic springs. Therefore, the motivation of this paper is to reveal nonlinear stiffness characteristics of Halbach array-based magnetic springs and investigate new magnetic springs with large-amplitude negative stiffness. Under the above-mentioned background, the novelty of the paper is to present the Halbach-cylinder magnetic spring (HCMS) for heavy-load QZS by using Halbach cylinders. The HCMS is composed of two coaxial Halbach cylinders, where the outer cylinder is fixed and the inner cylinder can move freely. Key metrics of the HCMS include the amplitude, the uniformity, and the displacement range of negative stiffness near the equilibrium position. The main challenges include deriving an analytical formula for nonlinear stiffness and designing proper structural configurations.

In summary, the main contributions of this work can be outlined as follows:

(1) The idea of Halbach array-based magnetic springs is introduced, so it is possible to generate large-amplitude negative stiffness by using magnetic structures.

(2) The magnetic forces and stiffness of all sixteen structures in four types of circular magnetic springs (CMSs) are obtained, which are used as cell units for building HCMSs.

(3) HCMSs are first proposed and the ‘*N-M*’-type HCMS is testified to generate larger negative stiffness than traditional magnetic rings.

The objective of this paper is to seek novel magnetic negative stiffness structures for heavy loads and provide a “building block” methodology for designing large-amplitude magnetic springs in engineering applications. The rest of this paper is organized as follows. Force and stiffness formulas of circular magnetic springs (CMSs) are analytically derived in Section 2. Based on them, the nonlinear stiffness of the ‘*N-M*’-type HCMS is built in Section 3. In Sections 4 and 5, the effects of geometric parameters on the nonlinear negative stiffness of basic CMSs and the 3-3-type HCMS are revealed, respectively. Then, a potential solution to HCMSs with larger-amplitude and wider-range negative stiffness is explored in Section 6. Finally, some conclusions are made in Section 7.

2. Force and Stiffness Characteristics of Circular Magnetic Springs

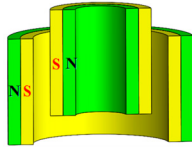
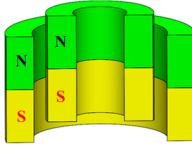
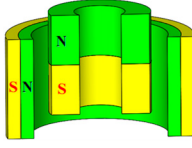
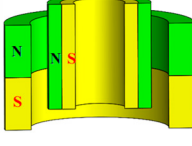
In this paper, the structure of the HCMS can be looked at as the combination of multiple pairs of coaxial magnetic rings. Therefore, it is necessary to investigate the characteristics of each kind of coaxial magnetic ring.

2.1. Different Configurations of Circular Magnetic Springs

A pair of coaxial magnetic rings forms a circular magnetic spring (CMS), including the inner and outer magnetic rings, and is also called the single-layer CMS. Each magnetic ring

can be radially or axially magnetized, so either the inner or the outer magnetic ring has two classes of main magnetizations. In total, there are four types of configurations for CMSs, including Type I (radial–radial magnetization), Type II (axial–axial magnetization), Type III (radially–axially perpendicular magnetization), and Type IV (axially–radially perpendicular magnetization). Furthermore, both the inner and the outer magnetic rings have two of their own magnetization directions, so each type of configuration has four structures. Here, one basic structure of each basic configuration is chosen optionally for a benchmark, and its denotation is listed in Table 1, where the arrows indicate the magnetization directions. Inside and outside radii of the inner magnetic ring are denoted as R_1 and R_2 . Inside and outside radii of the outer magnetic ring are denoted as R_3 and R_4 . Magnetic forces and stiffness of the four basic CMSs are denoted as $F_1 \sim F_4$ and $K_1 \sim K_4$, respectively.

Table 1. Four types of structural configurations for CMSs.

Description	Type	Basic Structure	Denotation	Magnetic Force	Stiffness
Radial–radial magnetization	Type I		OUT ← IN ←	F_1	K_1
Axial–axial magnetization	Type II		OUT ↑ IN ↑	F_2	K_2
Perpendicular magnetization (radial–axial)	Type III		OUT → IN ↑	F_3	K_3
Perpendicular magnetization (axial–radial)	Type IV		OUT ↑ IN →	F_4	K_4

Next, all sixteen structures of CMS are summarized in Table 2. According to Table 1, the magnetic forces and stiffness of the other three structures in each type of CMS can be obtained by referring to the basic structure.

Specifically, all denotations in Tables 1 and 2 are explained as follows: ‘OUT←’ indicates that the magnetization direction of the outer magnetic ring is radially outward from the inside. ‘OUT→’ indicates that the magnetization direction of the outer magnetic ring is radially inward from the outside. ‘OUT↑’ indicates that the magnetization direction of the outer magnetic ring is axially from bottom to top. ‘OUT↓’ indicates that the magnetization direction of the outer magnetic ring is axially from top to bottom. ‘IN→’ indicates that the magnetization direction of the inner magnetic ring is radially outward from the inside. ‘IN←’ indicates that the magnetization direction of the inner magnetic ring is radially inward from the outside. ‘IN↑’ indicates that the magnetization direction of the inner magnetic ring is axially from bottom to top. ‘IN↓’ indicates that the magnetization direction of the inner magnetic ring is axially from top to bottom.

Table 2. Magnetic force and stiffness of each configuration of CMSs.

Type	All Denotations	Magnetic Force	Stiffness
Type I	OUT \leftarrow IN \leftarrow	F_1	K_1
	OUT \leftarrow IN \rightarrow	$-F_1$	$-K_1$
	OUT \rightarrow IN \leftarrow	$-F_1$	$-K_1$
	OUT \rightarrow IN \rightarrow	F_1	K_1
Type II	OUT \uparrow IN \uparrow	F_2	K_2
	OUT \uparrow IN \downarrow	$-F_2$	$-K_2$
	OUT \downarrow IN \uparrow	$-F_2$	$-K_2$
	OUT \downarrow IN \downarrow	F_2	K_2
Type III	OUT \rightarrow IN \uparrow	F_3	K_3
	OUT \rightarrow IN \downarrow	$-F_3$	$-K_3$
	OUT \leftarrow IN \uparrow	$-F_3$	$-K_3$
	OUT \leftarrow IN \downarrow	F_3	K_3
Type IV	OUT \uparrow IN \rightarrow	F_4	K_4
	OUT \uparrow IN \leftarrow	$-F_4$	$-K_4$
	OUT \downarrow IN \rightarrow	$-F_4$	$-K_4$
	OUT \downarrow IN \leftarrow	F_4	K_4

2.2. Magnetic Force and Stiffness of Each Basic CMS

Generally speaking, different configurations of CMSs will have different stiffness characteristics. In order to reveal them in detail, it is necessary to obtain the magnetic force and stiffness between the inner and outer magnetic rings. The Amperian current model is more suitable for calculating forces between magnets [27], so it is adopted to analytically calculate the magnetic force and stiffness (i.e., $F_1 \sim F_4$ and $K_1 \sim K_4$) in this paper.

2.2.1. Type I CMSs

The detailed structure of Type I CMSs is shown in Figure 1a, where the inner magnetic ring is unconstrained and the outer magnetic ring is fixed. The heights of the inner and outer magnetic rings are denoted as $2h_1$, $2h_2$ and the residual flux densities of the inner and outer magnetic rings are denoted as B_{r1} , B_{r2} . The middle position of the outer magnetic ring is defined as the horizontal axis, and the distance between the two magnetic rings is denoted as z .

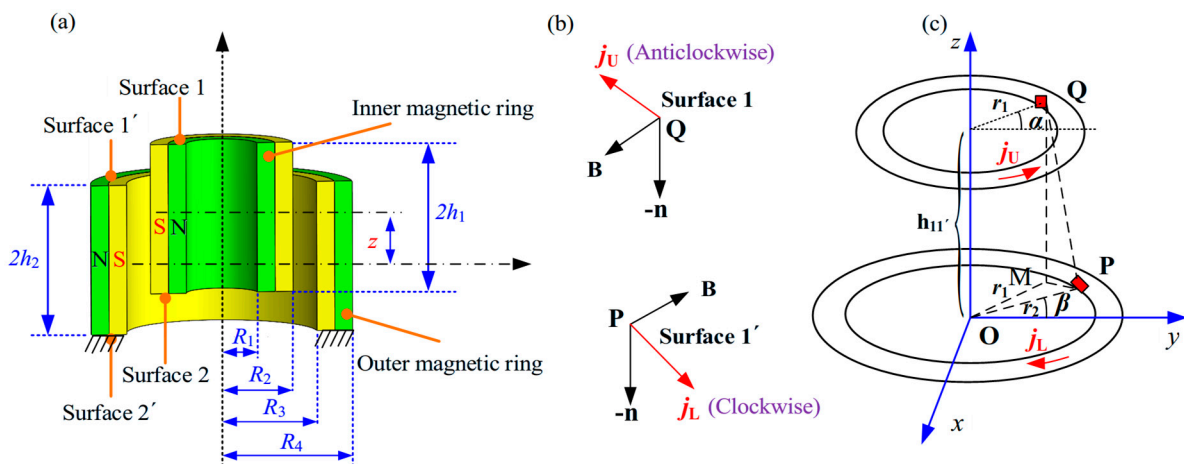


Figure 1. Schematic of Type I CMS: (a) structural configuration, (b) surface current directions, and (c) calculation of $F_{11'}(z)$.

According to the Amperian current model [27], the magnetic force of two magnets is equivalent to the interaction between equivalent currents distributed on the magnets. For

the magnetic ring with radial magnetization, the equivalent current only distributes on its upper and lower surfaces, and the surface current density can be written as

$$\mathbf{J} = -\mathbf{n} \times \mathbf{B} / \mu_0 \quad (1)$$

where \mathbf{n} is the unit vector normal to the surface, \mathbf{B} is the magnetic-field vector, $\mu_0 = 4\pi \times 10^{-7} \text{ V}\cdot\text{s}/(\text{A}\cdot\text{m})$ is the permeability of the vacuum, and ' \times ' denotes the vector product.

Furthermore, the upper and lower surfaces of the inner magnetic ring are denoted as 1 and 2, and the counterparts of the outer magnetic ring are denoted as 1' and 2', respectively. The radial force between the two surfaces is equal to zero due to the circular symmetry. The axial force between two surfaces is denoted as $F_{sv'}(z)$ ($s, v \in \{1, 2\}$), and $h_{sv'}(z)$ is the axial distance between two surfaces. Then, the magnetic force of Type I CMSs can be represented as the sum of the four axial forces.

$$F_1(z, 2h_1, 2h_2) = \sum_{s=1}^2 \sum_{v=1}^2 F_{sv'}(z) \quad (2)$$

Next, the calculation of $F_{11'}(z)$ is selected as an example. The current directions of surface 1 and 1' are shown in Figure 1b by using the right-hand rule. Their surface current densities are calculated as follows, based on Equation (1):

$$j_U = B_{r1} / \mu_0, \quad j_L = B_{r2} / \mu_0 \quad (3)$$

As shown in Figure 1c, a small current element $-j_U dr_1 d\mathbf{l}_1$ in the position $Q(r_1, \alpha, h_{11'})$ of surface 1 and one $j_L dr_2 d\mathbf{l}_2$ in the position $P(r_2, \beta, 0)$ of surface 1' are selected, respectively, where $|d\mathbf{l}_1| = r_1 d\alpha$, $|d\mathbf{l}_2| = r_2 d\beta$, α, β are the included angles between Q, P and the y axis, $d\alpha, d\beta$ denote the infinitesimal increments of α, β , and r_1, r_2 are the radii of Q and P points. According to the Biot–Savart law [28], the magnetic flux density at point Q produced by point P can be represented as Equation (4).

$$d\mathbf{B}_{11'} = \frac{\mu_0 j_L dr_2 d\mathbf{l}_2 \times \mathbf{PQ}_{11'}}{4\pi |\mathbf{PQ}_{11'}|^3} \quad (4)$$

Here, $\mathbf{PQ}_{11'}$ is the vector from point P to point Q, where $|\mathbf{PQ}_{11'}| = \sqrt{r_1^2 + r_2^2 + h_{11'}^2 - 2r_1 r_2 \cos(\beta - \alpha)}$ and $h_{11'} = h_1 + z - h_2$.

Then, the axial magnetic force exerted on $-j_U dr_1 d\mathbf{l}_1$ by $j_L dr_2 d\mathbf{l}_2$ can be written as Equation (5) by using Equations (3) and (4).

$$dF_{11'}(z) = \frac{B_{r1} B_{r2} r_1 r_2 h_{11'} \cos(\beta - \alpha) dr_1 dr_2 d\alpha d\beta}{4\pi \mu_0 |\mathbf{PQ}_{11'}|^3} \quad (5)$$

By performing integration on both sides of Equation (5), we will have

$$F_{11'}(z) = \frac{B_{r1} B_{r2}}{4\pi \mu_0} \int_{R_1}^{R_2} \int_{R_3}^{R_4} \int_0^{2\pi} \int_0^{2\pi} \frac{r_1 r_2 h_{11'}}{|\mathbf{PQ}_{11'}|^3} \cos(\beta - \alpha) dr_1 dr_2 d\alpha d\beta \quad (6)$$

Similar to $F_{11'}(z)$, other axial magnetic forces, including $F_{12'}(z)$, $F_{21'}(z)$, and $F_{22'}(z)$, can also be calculated as

$$F_{sv'}(z) = \frac{B_{r1} B_{r2}}{4\pi \mu_0} \int_{R_1}^{R_2} \int_{R_3}^{R_4} \int_0^{2\pi} \int_0^{2\pi} (-1)^{s+v} \frac{r_1 r_2 h_{sv'}}{|\mathbf{PQ}_{sv'}|^3} \cos(\beta - \alpha) dr_1 dr_2 d\alpha d\beta \quad (7)$$

where $h_{sv'} = z - (-1)^s h_1 + (-1)^v h_2$ and $|\mathbf{PQ}_{sv'}| = \sqrt{r_1^2 + r_2^2 + h_{sv'}^2 - 2r_1 r_2 \cos(\beta - \alpha)}$, $s, v \in \{1, 2\}$.

According to the directions of two surface currents, $F_{11'}$, $F_{22'}$ are the repulsive forces and $F_{12'}$, $F_{21'}$ are the attractive forces. By combining Equations (2) and (7), $F_1(z, 2h_1, 2h_2)$ can be calculated as

$$F_1(z, 2h_1, 2h_2) = \frac{B_{r1} B_{r2}}{4\pi\mu_0} \sum_{s=1}^2 \sum_{v=1}^2 \int_{R_1}^{R_2} \int_{R_3}^{R_4} \int_0^{2\pi} \int_0^{2\pi} (-1)^{s+v} \frac{r_1 r_2 h_{sv'}}{|\mathbf{PQ}_{sv'}|^3} \cos(\beta - \alpha) dr_1 dr_2 d\alpha d\beta \quad (8)$$

Then, the stiffness K_1 can be obtained as

$$K_1(z, 2h_1, 2h_2) = -\frac{dF_1}{dz} = \frac{B_{r1} B_{r2}}{4\pi\mu_0} \sum_{s=1}^2 \sum_{v=1}^2 \int_{R_1}^{R_2} \int_{R_3}^{R_4} \int_0^{2\pi} \int_0^{2\pi} (-1)^{s+v} \frac{r_1 r_2 (3h_{sv'}^2 - |\mathbf{PQ}_{sv'}|^2)}{|\mathbf{PQ}_{sv'}|^5} \cos(\beta - \alpha) dr_1 dr_2 d\alpha d\beta \quad (9)$$

2.2.2. Type II CMSs

The detailed structure of Type II CMSs is shown in Figure 2a, where the geometric configuration is similar to that in Figure 1a. The inner and outer surfaces of the inner and outer magnetic rings are denoted as 3, 3', 4, and 4', respectively. The radial force between the two surfaces is also equal to zero due to the circular symmetry. The axial force between two surfaces is denoted as $F_{sv'}(z)$ ($s, v \in \{3, 4\}$) and then the magnetic force of Type II CMSs can be calculated as

$$F_2(z, 2h_1, 2h_2) = \sum_{s=3}^4 \sum_{v=3}^4 F_{sv'}(z) \quad (10)$$

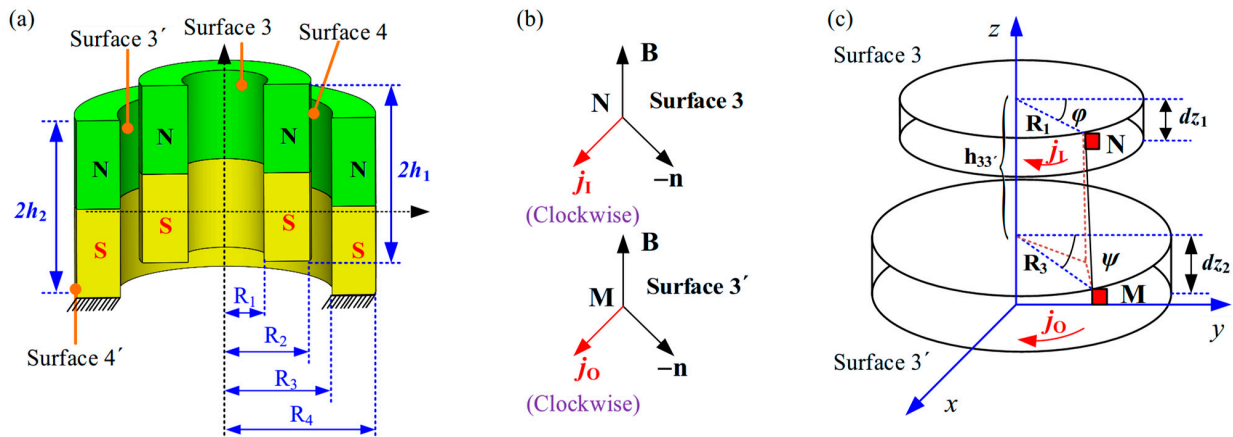


Figure 2. Schematic of Type II CMS: (a) structural configuration, (b) surface current directions, and (c) calculation of $F_{33'}(z)$.

Next, the calculation of $F_{33'}(z)$ is selected as an example. The current directions of surface 3 and 3' are shown in Figure 2b by using the right-hand rule. $h_{33'}(z)$ is the axial distance between the two surfaces. The axial magnetic force exerted on $j_1 R_1 d\varphi dz_1$ at point N by $j_0 R_3 d\psi dz_2$ at point M is

$$dF_{33'}(z) = j_1 R_1 d\varphi dz_1 \times d\mathbf{B}_{33'} \quad (11)$$

where $d\mathbf{B}_{33'} = \mu_0 j_0 R_3 d\psi dz_2 \times \mathbf{MN}_{33'} / (4\pi |\mathbf{MN}_{33'}|^3)$ is the magnetic flux density at point M produced by $j_0 R_3 d\psi dz_2$ at point N; $|\mathbf{MN}_{33'}| = \sqrt{R_1^2 + R_3^2 + h_{33'}^2 - 2R_1 R_3 \cos(\psi - \varphi)}$ is

the vector from point M to point N ; and $h_{33'} = z_1 + z - z_2$ is the axial distance from surface 3 to surface $3'$.

The axial magnetic force $F_{33'}(z)$ can be obtained as

$$F_{33'}(z) = -\frac{B_{r1}B_{r2}}{4\pi\mu_0} \int_0^{2\pi} \int_0^{2\pi} \int_{-h_1}^{h_1} \int_{-h_2}^{h_2} \frac{R_1R_3h_{33'} \cos(\psi - \varphi)}{|\mathbf{MN}_{33'}|^3} dz_1 dz_2 d\varphi d\psi \quad (12)$$

Similar to $F_{33'}(z)$, axial magnetic forces $F_{34'}(z)$, $F_{43'}(z)$, and $F_{44'}(z)$ can also be calculated as

$$F_{sv'}(z) = -(-1)^{s+v} \frac{B_{r1}B_{r2}}{4\pi\mu_0} \int_0^{2\pi} \int_0^{2\pi} \int_{-h_1}^{h_1} \int_{-h_2}^{h_2} \frac{R_{s-2}R_v h_{sv'} \cos(\psi - \varphi)}{|\mathbf{MN}_{sv'}|} dz_1 dz_2 d\varphi d\psi \quad (13)$$

where $|\mathbf{MN}_{sv'}| = \sqrt{R_s^2 + R_v^2 + h_{sv'}^2 - 2R_{s-2}R_v \cos(\psi - \varphi)}$ and $h_{sv'} = z - (-1)^s z_1 + (-1)^v z_2$, $s, v \in \{3, 4\}$.

Combining Equations (10) and (11), $F_2(z, 2h_1, 2h_2)$ can be rewritten as

$$F_2(z, 2h_1, 2h_2) = -\frac{B_{r1}B_{r2}}{4\pi\mu_0} \sum_{s=3}^4 \sum_{v=3}^4 \int_{-h_1}^{h_1} \int_{-h_2}^{h_2} \int_0^{2\pi} \int_0^{2\pi} (-1)^{s+v} \frac{R_{s-2}R_v h_{sv'}}{|\mathbf{MN}_{sv'}|^3} \cos(\psi - \varphi) dz_1 dz_2 d\varphi d\psi \quad (14)$$

Then, the stiffness K_2 can be obtained as

$$K_2(z, 2h_1, 2h_2) = -\frac{B_{r1}B_{r2}}{4\pi\mu_0} \sum_{s=3}^4 \sum_{v=3}^4 \int_{-h_1}^{h_1} \int_{-h_2}^{h_2} \int_0^{2\pi} \int_0^{2\pi} (-1)^{s+v} \frac{(|\mathbf{MN}_{sv'}|^2 - 3h_{sv'}^2) R_{s-2}R_v}{|\mathbf{MN}_{sv'}|^3} \cos(\psi - \varphi) dz_1 dz_2 d\varphi d\psi \quad (15)$$

2.2.3. Type III CMSs and Type IV CMSs

The structures of Type III and Type IV CMSs are shown in Figure 3. By referring to the above calculation method, $F_3(z, 2h_1, 2h_2)$ and K_3 can be formulated as

$$F_3(z, 2h_1, 2h_2) = \frac{B_{r1}B_{r2}}{4\pi\mu_0} \sum_{s=3}^4 \sum_{v=1}^2 \int_0^{2\pi} \int_0^{2\pi} \int_{R_3-h_1}^{R_4} \int_{-h_1}^{h_1} (-1)^{s+v} \frac{r_2 R_{s-2} h_{sv'}}{|\mathbf{MN}_{sv'}|^3} \cos(\varphi - \beta) d\beta d\varphi dr_2 dz_1 \quad (16)$$

$$K_3(z, 2h_1, 2h_2) = \frac{B_{r1}B_{r2}}{4\pi\mu_0} \sum_{s=3}^4 \sum_{v=1}^2 \int_0^{2\pi} \int_0^{2\pi} \int_{R_3-h_1}^{R_4} \int_{-h_1}^{h_1} (-1)^{s+v} \frac{r_2 R_{s-2} h_{sv'}}{|\mathbf{MN}_{sv'}|^3} \cos(\varphi - \beta) d\beta d\varphi dr_2 dz_1 \quad (17)$$

where $|\mathbf{MN}_{sv'}| = \sqrt{R_{s-2}^2 + r_2^2 + h_{sv'}^2 - 2R_{s-2}r_2 \cos(\varphi - \beta)}$ and $h_{sv'} = z_1 + z + (-1)^v h_2$, $s \in \{3, 4\}$, $v \in \{1, 2\}$.

Similarly, $F_4(z, 2h_1, 2h_2)$ and K_4 can also be formulated as

$$F_4(z, 2h_1, 2h_2) = -\frac{B_{r1}B_{r2}}{4\pi\mu_0} \sum_{s=1}^2 \sum_{v=3}^4 \int_0^{2\pi} \int_0^{2\pi} \int_{R_1-h_2}^{R_2} \int_{-h_2}^{h_2} (-1)^{s+v} \frac{r_1 R_v h_{sv'}}{|\mathbf{MN}_{sv'}|^3} \cos(\psi - \alpha) d\psi d\alpha dr_1 dz_2 \quad (18)$$

$$K_4(z, 2h_1, 2h_2) = \frac{B_{r1}B_{r2}}{4\pi\mu_0} \sum_{s=1}^2 \sum_{v=3}^4 \int_0^{2\pi} \int_0^{2\pi} \int_{R_1-h_2}^{R_2} \int_{-h_2}^{h_2} (-1)^{s+v} \frac{(|\mathbf{MN}_{sv'}|^2 - 3h_{sv'}^2) r_1 R_v}{|\mathbf{MN}_{sv'}|^5} \cos(\psi - \alpha) d\psi d\alpha dr_1 dz_2 \quad (19)$$

where $|\mathbf{MN}_{sv'}| = \sqrt{R_v^2 + r_1^2 + h_{sv'}^2 - 2R_v r_1 \cos(\psi - \varphi)}$ and $h_{sv'} = z - z_2 + (-1)^s h_1$, $s \in \{1, 2\}$, $v \in \{3, 4\}$.

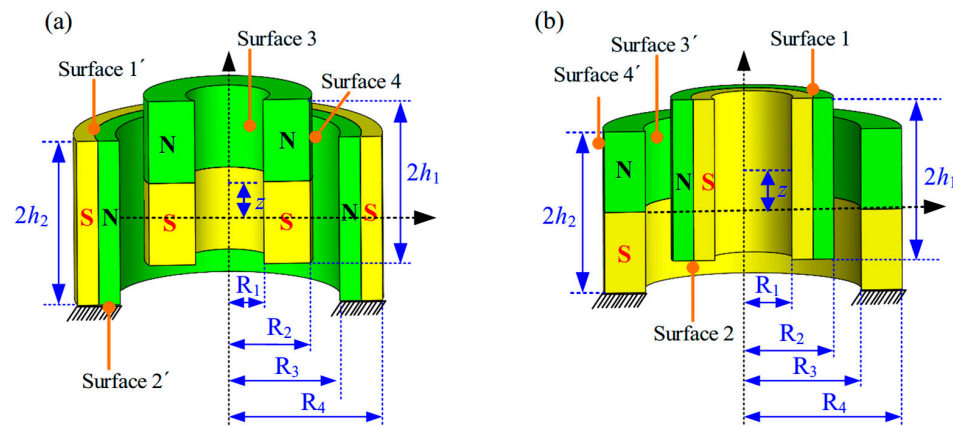


Figure 3. Structures of (a) Type III and (b) Type IV CMSs.

Finally, the bullet list of key variables in the above equations is shown in Table 3.

Table 3. The bullet list of key variables.

Symbol	Physical Meaning	Unit
\mathbf{B}	The magnetic-field vector	—
B_{r1}	The residual flux density of the inner magnetic ring	T
B_{r2}	The residual flux density of the outer magnetic ring	T
$F_{sv'}(z)$	The axial force between the surface s and the surface v'	N
h_1	The half-height of the inner magnetic ring	m
h_2	The half-height of the outer magnetic ring	m
\mathbf{J}	The surface current density vector	—
j_U	The surface current density of surface 1	A/m ²
j_L	The surface current density of surface 1'	A/m ²
j_I	The surface current density of surface 3	A/m ²
j_O	The surface current density of surface 3'	A/m ²
\mathbf{n}	The unit normal vector	—
R_1	The inside radius of the inner magnetic ring	m
R_2	The outside radius of the inner magnetic ring	m
R_3	The inside radius of the outer magnetic ring	m
R_4	The outside radius of the outer magnetic ring	m
r_1	The radius of the Q point	m
r_2	The radius of the P point	m
\times	The vector product	—
μ_0	The permeability of the vacuum	V·s/(A·m)
α	The included angles between Q and the y axis	rad
β	The included angles between P and the y axis	rad

3. Analytical Stiffness of Halbach-Cylinder Magnetic Spring

3.1. Basic Configuration of an HCMS

A Halbach array is a special arrangement of permanent magnets that enhances the magnetic field on one side of the array, while canceling the field to near zero on the other side. This is achieved by having a spatially rotating pattern of magnetization, which can be understood by observing the magnetic flux distribution shown in Figure 4. In Figure 4a, the pattern of magnetization rotates clockwise, so that the left magnetic field is enhanced while the right field is canceled. In Figure 4b, the pattern of magnetization rotates anticlockwise, so that the right magnetic field is enhanced while the left field is canceled. To date, two types of Halbach arrays have been proposed, namely the flat Halbach array [24] and the Halbach cylinder [26].

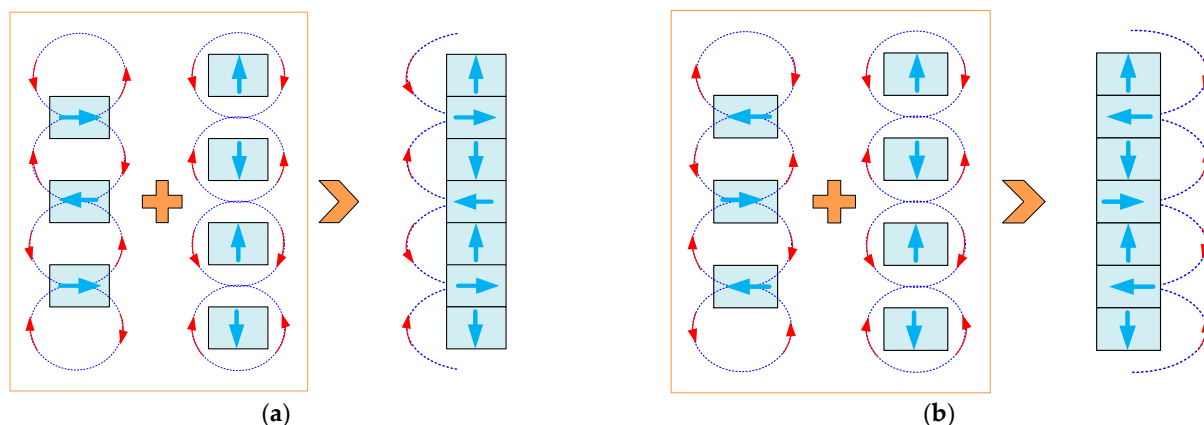


Figure 4. Formation mechanism of Halbach array: (a) left-side enhancement and (b) right-side enhancement.

Based on the mechanism in Figure 4, two coaxial Halbach cylinders are utilized to build an HCMS in this paper. That is to say, the HCMS is composed of the inner Halbach cylinder and the outer Halbach cylinder. In order to generate a larger magnetic force of the HCMS, the magnetization direction of the outer Halbach cylinder should change anticlockwise from top to bottom, while it should change clockwise for the inner Halbach cylinder. According to Figure 4, the magnetic field between the inner and outer Halbach cylinders can be greatly enhanced.

In this paper, an HCMS is denoted as an ‘ N - M ’ type (N , M should be odd), which means that the outer Halbach cylinder consists of N -layer magnetic rings and the inner Halbach cylinder consists of M -layer magnetic rings. Then, there are total NM CMSs in the HCMS. Therefore, the magnetic force and stiffness of the ‘ N - M ’-type HCMS can be written as

$$F_H(z) = \sum_{i=1}^{NM} \tilde{F}_i(z) \quad (20)$$

$$K_H(z) = -\partial F_H(z) / \partial z$$

where $\tilde{F}_i(z)$ is the magnetic force of the i th CMS, which can refer to Section 2. As for each ‘ N - M ’-type HCMS, both the inner and the outer Halbach cylinders have four different configurations according to the magnetization directions, leading to sixteen structures. A representative structure of the 3-3-type HCMS is shown in Figure 5. The vertical center position of the outer Halbach cylinder is denoted as the horizontal axis, and the displacement between the inner and outer Halbach cylinders is denoted as z .

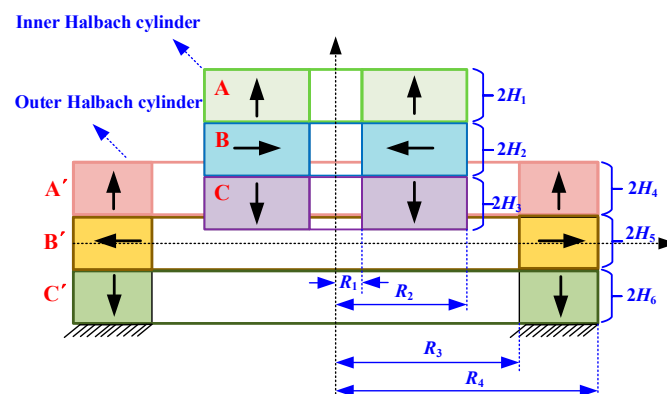


Figure 5. Schematic structure of the 3-3-type HCMS.

3.2. Stiffness Formulation of the 3-3-Type HCMS

As for the 3-3-type HCMS in Figure 5, its magnetic force can be calculated as

$$F_H^{3-3}(z) = \sum_{i=A}^C \sum_{j=A'}^{C'} F_{ij}(z) \quad (21)$$

where $F_{ij}(z)$ denotes the magnetic force of the CMS, consisting of the i and j magnetic rings.

Furthermore, $F_{ij}(z)$ can be calculated using Equation (22) based on Table 2.

$$\begin{aligned} F_{AA'} &= F_2(z + H_1 + H_2 - H_4 - H_5, 2H_1, 2H_4) \\ F_{AB'} &= -F_3(z + H_1 + H_2, 2H_1, 2H_5) \\ F_{AC'} &= -F_2(z + H_1 + H_2 + H_5 + H_6, 2H_1, 2H_6) \\ F_{BA'} &= -F_4(z - H_4 - H_5, 2H_2, 2H_4) \\ F_{BB'} &= F_1(z, 2H_2, 2H_5) \\ F_{BC'} &= F_4(z + H_5 + H_6, 2H_2, 2H_6) \\ F_{CA'} &= -F_2(z - H_2 - H_3 - H_4 - H_5, 2H_3, 2H_4) \\ F_{CB'} &= F_3(z - H_2 - H_3, 2H_3, 2H_5) \\ F_{CC'} &= F_2(z + H_4 + H_5 - H_2 - H_3, 2H_3, 2H_6) \end{aligned} \quad (22)$$

By combining Equations (21) and (22), $F_H^{3-3}(z)$ can be written as

$$\begin{aligned} F_H^{3-3}(z) &= F_2(z + H_1 + H_2 - H_4 - H_5, 2H_1, 2H_4) - F_3(z + H_1 + H_2, 2H_1, 2H_5) - \\ &F_2(z + H_1 + H_2 + H_5 + H_6, 2H_1, 2H_6) - F_4(z - H_4 - H_5, 2H_2, 2H_4) + \\ &F_1(z, 2H_2, 2H_5) + F_4(z + H_5 + H_6, 2H_2, 2H_6) - F_2(z - H_2 - H_3 - H_4 - H_5, 2H_3, 2H_4) \\ &+ F_3(z - H_2 - H_3, 2H_3, 2H_5) + F_2(z + H_4 + H_5 - H_2 - H_3, 2H_3, 2H_6) \end{aligned} \quad (23)$$

Then, the stiffness formulation of the 3-3-type HCMS can be written as

$$\begin{aligned} K_H^{3-3}(z) &= K_2(z + H_1 + H_2 - H_4 - H_5, 2H_1, 2H_4) - K_3(z + H_1 + H_2, 2H_1, 2H_5) - \\ &K_2(z + H_1 + H_2 + H_5 + H_6, 2H_1, 2H_6) - K_4(z - H_4 - H_5, 2H_2, 2H_4) + \\ &K_1(z, 2H_2, 2H_5) + K_4(z + H_5 + H_6, 2H_2, 2H_6) - K_2(z - H_2 - H_3 - H_4 - H_5, 2H_3, 2H_4) \\ &+ K_3(z - H_2 - H_3, 2H_3, 2H_5) + K_2(z + H_4 + H_5 - H_2 - H_3, 2H_3, 2H_6) \end{aligned} \quad (24)$$

Finally, the stiffness characteristics of the 3-3-type HCMS can be analytically investigated based on Equations (9), (15), (17), (19) and (24).

4. Parametric Analysis of Negative Stiffness of Basic CMSs

In this section, the analytical formulas in Section 2 are utilized to reveal the stiffness characteristics of each basic CMS. Geometric parameter values of the CMS are listed in Table 4 and $B_{r1} = B_{r2} = 1 \text{ T}$.

Table 4. Parameter values of the CMS.

Parameter	R_1	R_2	R_3	R_4	h_1	h_2
Value	10 mm	17.5 mm	22.5 mm	30 mm	10 mm	10 mm

4.1. Stiffness Curves of the Four Basic CMSs

Magnetic force curves of the four basic CMSs are calculated and shown in Figure 6. The following can be seen: (i) In Figure 6a,b, The force equilibrium positions of Type I and Type II CMSs are located on the horizontal axis (i.e., $z = 0$). However, the magnetic force of the Type III CMS in Figure 6c reaches the maximum positive value (repulsive force) at $z = 0$ and the magnetic force of the Type IV CMS in Figure 6d reaches the maximum

negative value (attractive force) at $z = 0$. (ii) Magnetic force curves of Type I and Type II CMSs have asimilar sine-like shape, and the latter has the larger peak value. (iii) Magnetic force curves of Type III and Type IV CMSs are symmetrical in terms of the axis of $z = 0$, but the directions are reversed.

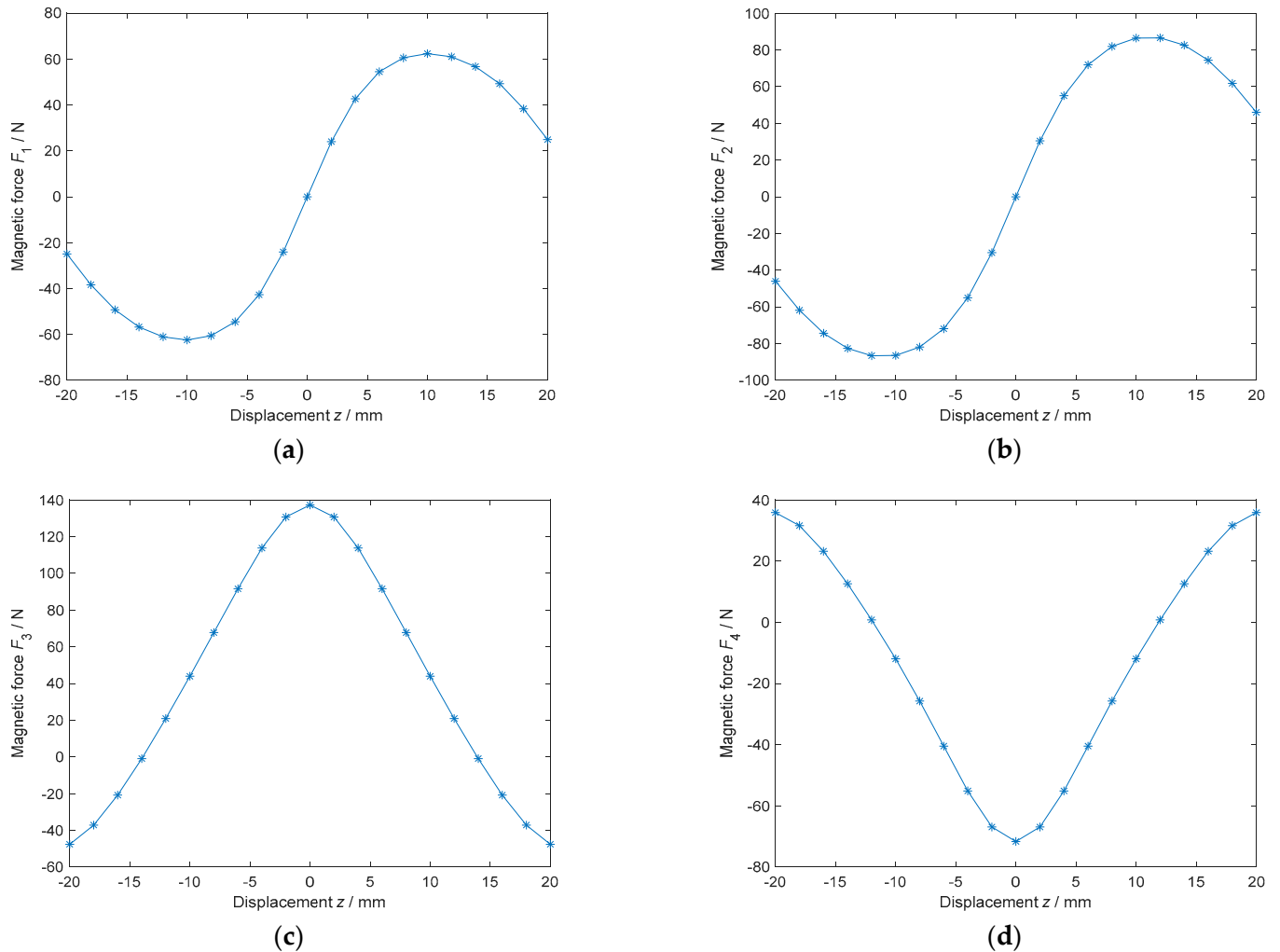


Figure 6. Magnetic force curves of the (a) Type I, (b) Type II, (c) Type III, and (d) Type IV CMSs.

Next, the stiffness curves of four basic CNSs are calculated and shown in Figure 7. The following can be seen: (i) All stiffness curves are nonlinear. (ii) Both Type I and Type II CMSs have symmetrical negative stiffness near $z = 0$. The stiffness of Type III CMSs is negative when $z \in [-10, 0]$, and the stiffness of Type IV CMSs is negative when $z \in [0, 10]$. (iii) Type II CMSs have the largest negative stiffness and the widest displacement range of negative stiffness, but Type IV CMSs have the best uniformity of negative stiffness. Therefore, it can be concluded that any CMS has negative stiffness with different displacement ranges.

Considering the equilibrium position, Type II CMSs may be the most suitable for compact design. In real-world applications, the amplitude, the displacement range, and the uniformity of negative stiffness are three important metrics of QZS vibration isolators. Consequently, it is valuable to investigate the effects of key geometric parameters on the three metrics of K_2 , including the coaxial thickness, the radial thickness, and the gap between the two magnetic rings. R_1 and R_4 are fixed.

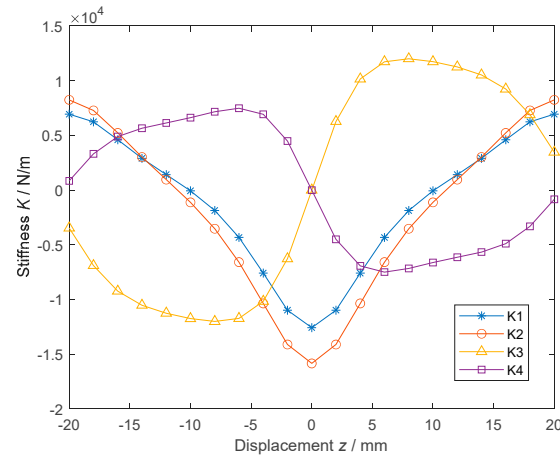


Figure 7. Stiffness curves of the four basic CMSs.

4.2. Effects of the Axial Thickness on K_2

Firstly, the axial thickness ($h_2 = 5\text{ mm}$) of the outer magnet is fixed, and the axial thickness (h_1) of the inner magnet is defined as $h_1 = a \times h_2$. Here, a is the axial thickness ratio, which is chosen as $\{0.4, 0.6, 0.8, 1.0, 1.2\}$. In this case, the curves of K_2 are plotted in Figure 8a. It can be seen that (i) as a increases, the displacement range and uniformity of negative stiffness also increase, and (ii) as a increases, the amplitude of negative stiffness first increases and then decreases. It will reach the maximum value when $a = 1.0$. Furthermore, K_2 , with different axial thicknesses ($a = 1.0$), is calculated as shown in Figure 8b. The results show that (i) as the axial thickness increases, the displacement range of negative stiffness will also increase, and the uniformity hardly changes, and (ii) as the axial thickness increases, the amplitude of negative stiffness first increases and then decreases.

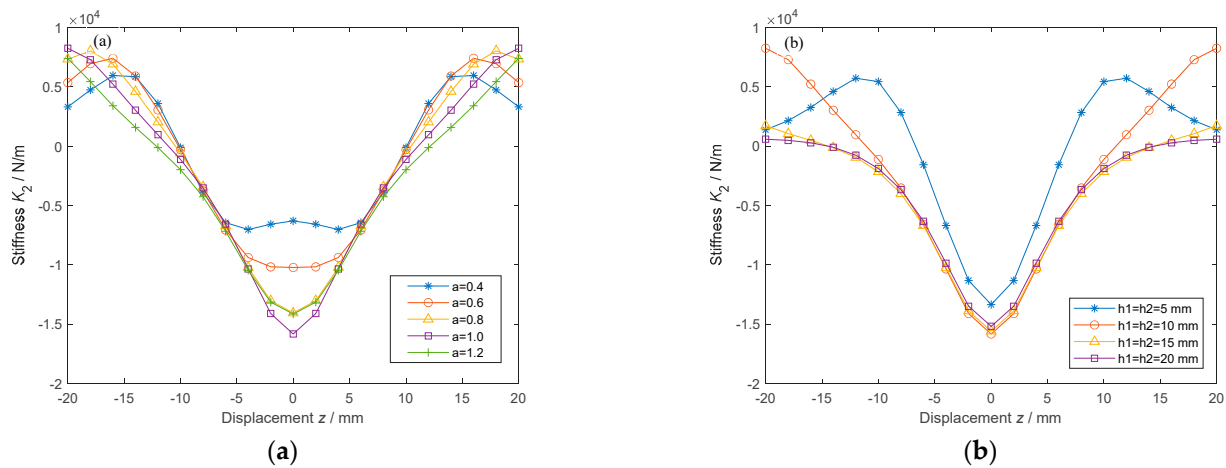


Figure 8. Effects of (a) the relative and (b) the absolute axial thickness on K_2 .

4.3. Effects of the Radial Thickness Ratio on K_2

Secondly, the radial thickness of the inner magnetic ring and the gap are fixed. That is to say, $R_1 \sim R_3$ are fixed and $R_4 = R_3 + g \times (R_2 - R_1)$. Here, g is the radial thickness ratio, which is chosen as $\{0.4, 0.6, 0.8, 1.0, 1.2\}$. In this case, the curves of K_2 are plotted in Figure 9. It can be seen that (i) with the increase in g , the displacement range of negative stiffness hardly changes, and (ii) with the increase in g , the amplitude of negative stiffness will also increase, but the uniformity of negative stiffness will decrease.

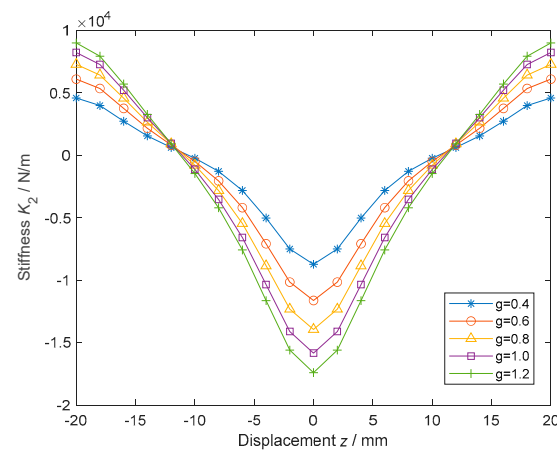


Figure 9. Effects of g on K_2 .

4.4. Effects of the Gap (d) on K_2

Thirdly, the coaxial and radial thicknesses of the two magnetic rings are fixed. That is to say, $h_1, h_2, R_1, R_2, R_4 - R_3$ are fixed and $R_3 = R_2 + d$. Here, the values of d are chosen as $\{2, 4, 6, 8, 10\}$. In this case, the curves of K_2 are plotted in Figure 10. It can be seen that both the displacement range and the uniformity of negative stiffness will increase with d , but the amplitude will decrease with d .

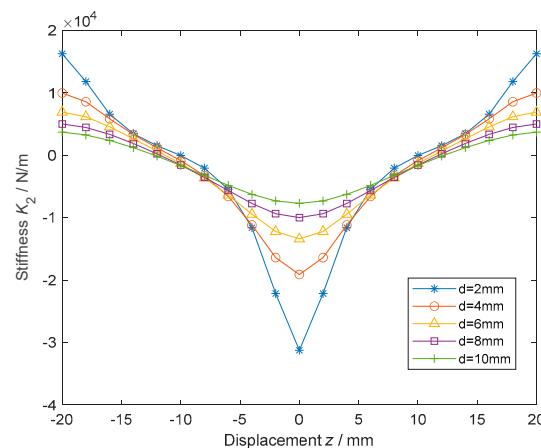


Figure 10. Effects of d on K_2 .

By referring to Figures 7–10, it can be concluded that (i) the amplitude of negative stiffness conflicts with the uniformity of negative stiffness, and there should be a trade-off design in practice, and that (ii) two magnetic rings with the same optimal coaxial thickness can lead to the largest amplitude of negative stiffness.

5. Parametric Analysis of Negative Stiffness of the 3-3-Type HCMS

In this section, the analytical formulas in Section 3 are utilized to reveal the stiffness characteristics of the 3-3-type HCMS. Its geometric parameter values are listed in Table 5 and $B_{r1} = B_{r2} = 1$.

Table 5. Parameter values of the 3-3-type HCMS.

Parameter	R_1	R_2	R_3	R_4	$H_1 \sim H_6$
Value	10 mm	17.5 mm	22.5 mm	30 mm	5 mm

5.1. Validation of the Analytical Model by Finite Element Modeling

In order to validate the analytical formulas of magnetic force and stiffness in Equations (23) and (24), COMSOL Multiphysics® software (v6.3, COMSOL, Inc., Stockholm, Sweden) is utilized for finite element simulations on magnetic forces (stiffness cannot be directly simulated). The finite element model (FEM) of the 3-3-type HCMS in Figure 5 is built as shown in Figure 11a, where the inner and outer Halbach cylinders are automatically meshed by using the tetrahedral elements. Then, parametric-sweep simulations are carried out over the distance z and the corresponding forces are simulated and recorded. At the same time, magnetic force and stiffness curves of the same 3-3-type HCMS are calculated by using the analytical formulas. Next, the analytical and simulated magnetic force curves are compared in Figure 11b, and the stiffness curve is shown in Figure 11c. The following can be seen: (i) As for the magnetic force, the analytical and simulation results are almost consistent. This indicates that the proposed analytical model is accurate and feasible. (ii) The magnetic force is equal to zero at $z = 0$. That is to say, the force equilibrium position is located on the horizontal axis. The magnetic force curve has a sine-like shape near the equilibrium position. (iii) The stiffness curve is symmetrical in terms of the axis of $z = 0$. In particular, the stiffness is negative near the equilibrium position, which proves that the 3-3-type HCMS can generate a negative stiffness.

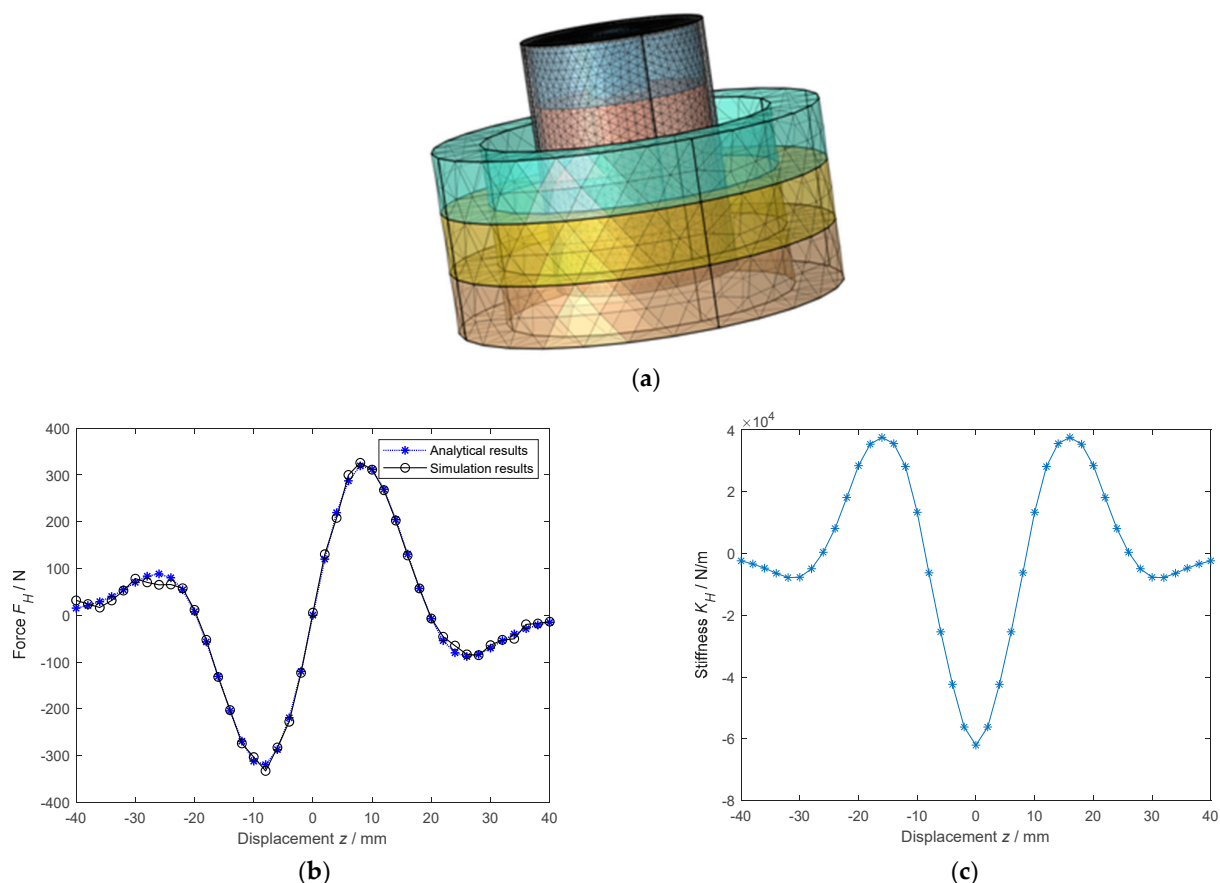


Figure 11. (a) FEM, (b) magnetic force, and (c) stiffness of the 3-3-type HCMS.

5.2. Comparison of the 3-3-Type HCMS with a Traditional Single-Layer CMS

In order to validate the superiority of the 3-3-type HCMS, traditional Type I CMSs and Type II CMSs with the same geometric dimensions are also considered and compared. Then, their stiffness curves are compared in Figure 12. It is obvious that the amplitude of negative stiffness of the 3-3-type HCMS at $z = 0$ is almost five times that of Type I CMSs and Type II CMSs. The results verify that a large-amplitude negative stiffness can

be generated by the HCMS. Furthermore, it is valuable to investigate the effects of key geometric parameters on the three metrics of K_H^{3-3} .

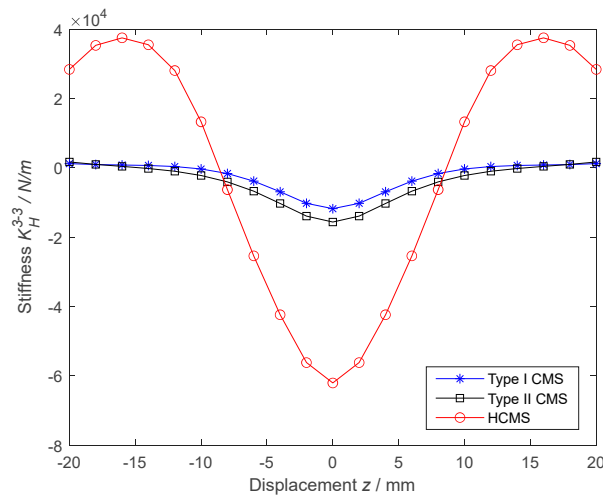


Figure 12. Comparisons of the 3-3-type HCMS with traditional Type I and Type II CMSs.

5.3. Effects of Geometric Parameters on K_H^{3-3}

Firstly, $H_1 = H_2 = H_3 = H = 5$ mm and $H_4 = H_5 = H_6 = a \times H$. The relation curve between K_H^{3-3} and a is plotted in Figure 13a. Secondly, $R_1 \sim R_3$ are fixed and $R_4 = R_3 + g \times (R_2 - R_1)$. The relation curve between K_H^{3-3} and g is plotted in Figure 13b. Thirdly, $H_1 \sim H_6, R_1, R_2, R_4 - R_3$ are fixed and $R_3 = R_2 + d$. The relation curve between K_H^{3-3} and d is plotted in Figure 13c. Compared with Figures 8–10, similar trends can be seen in Figure 13.

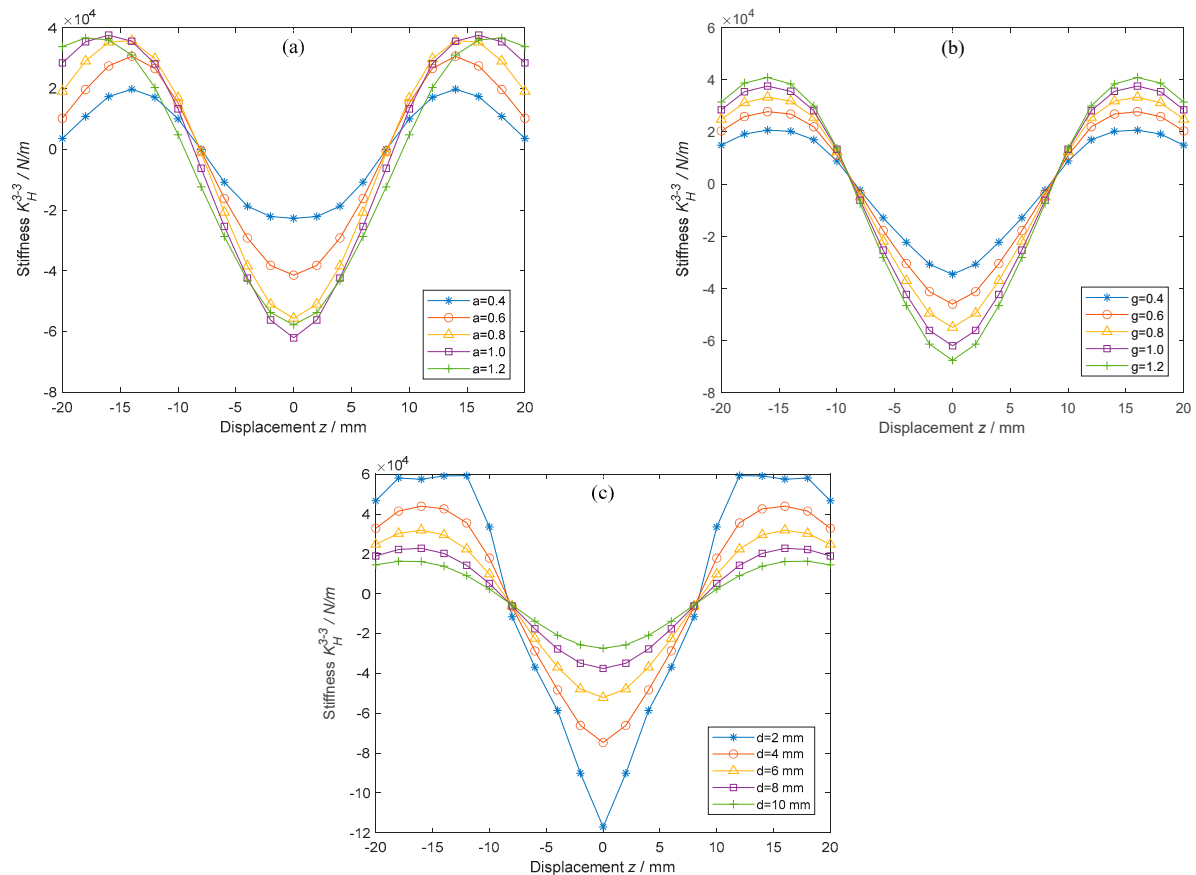


Figure 13. The curves of K_H^{3-3} under different (a) a , (b) g , and (c) d .

5.4. Nonlinear Stiffness Characteristics of All 3-3-Type HCMSs

As mentioned before, each ' N - M '-type HCMS has sixteen structural configurations. Here, all structural configurations of the 3-3-type HCMS are shown in Figure 14. It can be seen that the first structural configuration matches the one shown in Figure 5. The same geometric values in Table 4 are adopted, and the stiffness curves are plotted in Figure 15. The results show the following: (i) There are only eight different nonlinear stiffness curves due to the structural duality. (ii) Each 3-3-type HCMS has negative stiffness, but the displacement range of negative stiffness is different. Furthermore, the configurations on the main diagonal (i.e., the diagonal, red dotted line) have negative stiffness near $z = 0$ and are useful for compact design. (iii) The amplitude of negative stiffness of any 3-3-type HCMS is larger than that of a single-layer magnetic spring. Both the first and the eleventh 3-3-type HCMS have the largest amplitude of negative stiffness at $z = 0$.

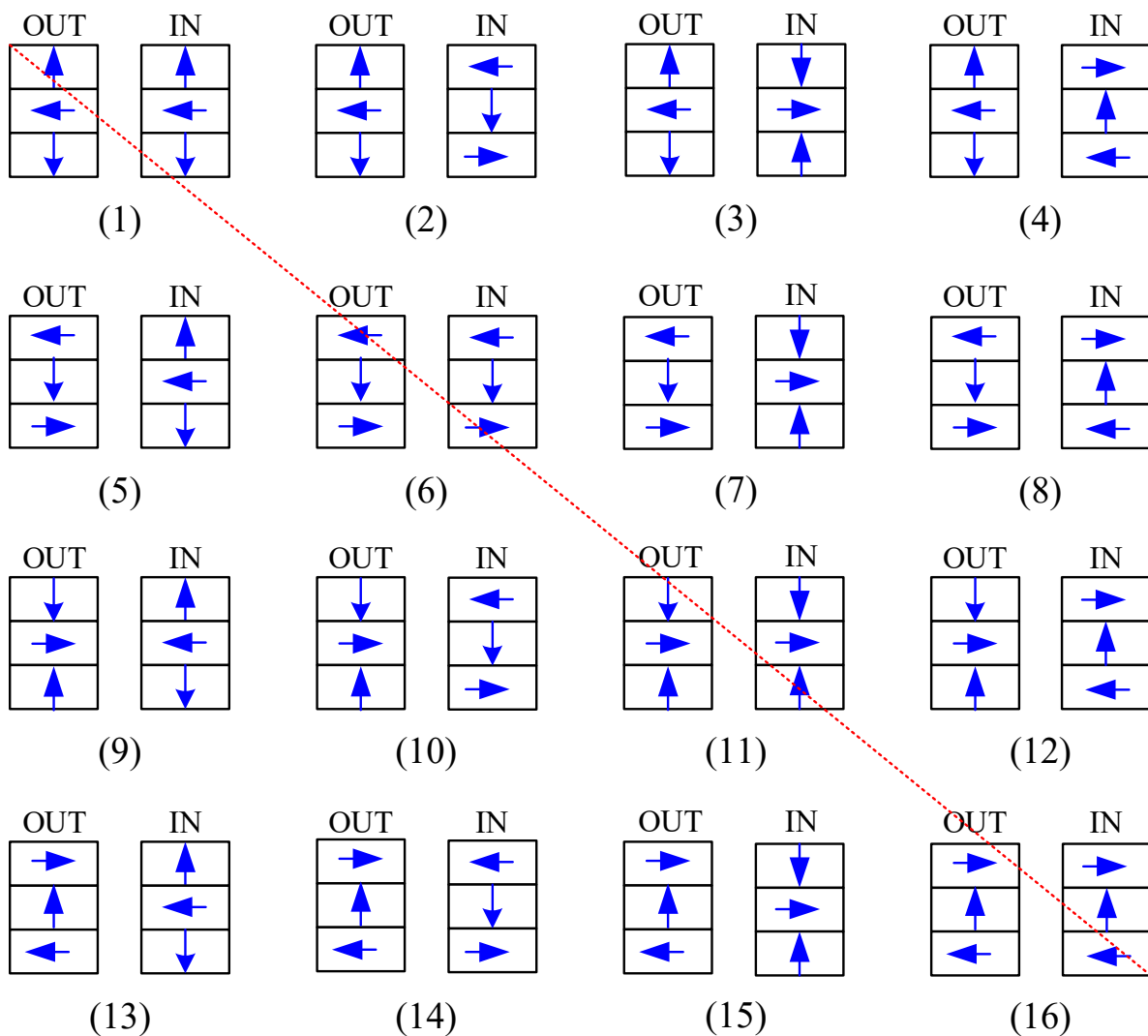


Figure 14. Sixteen structural configurations of the 3-3-type HCMS.

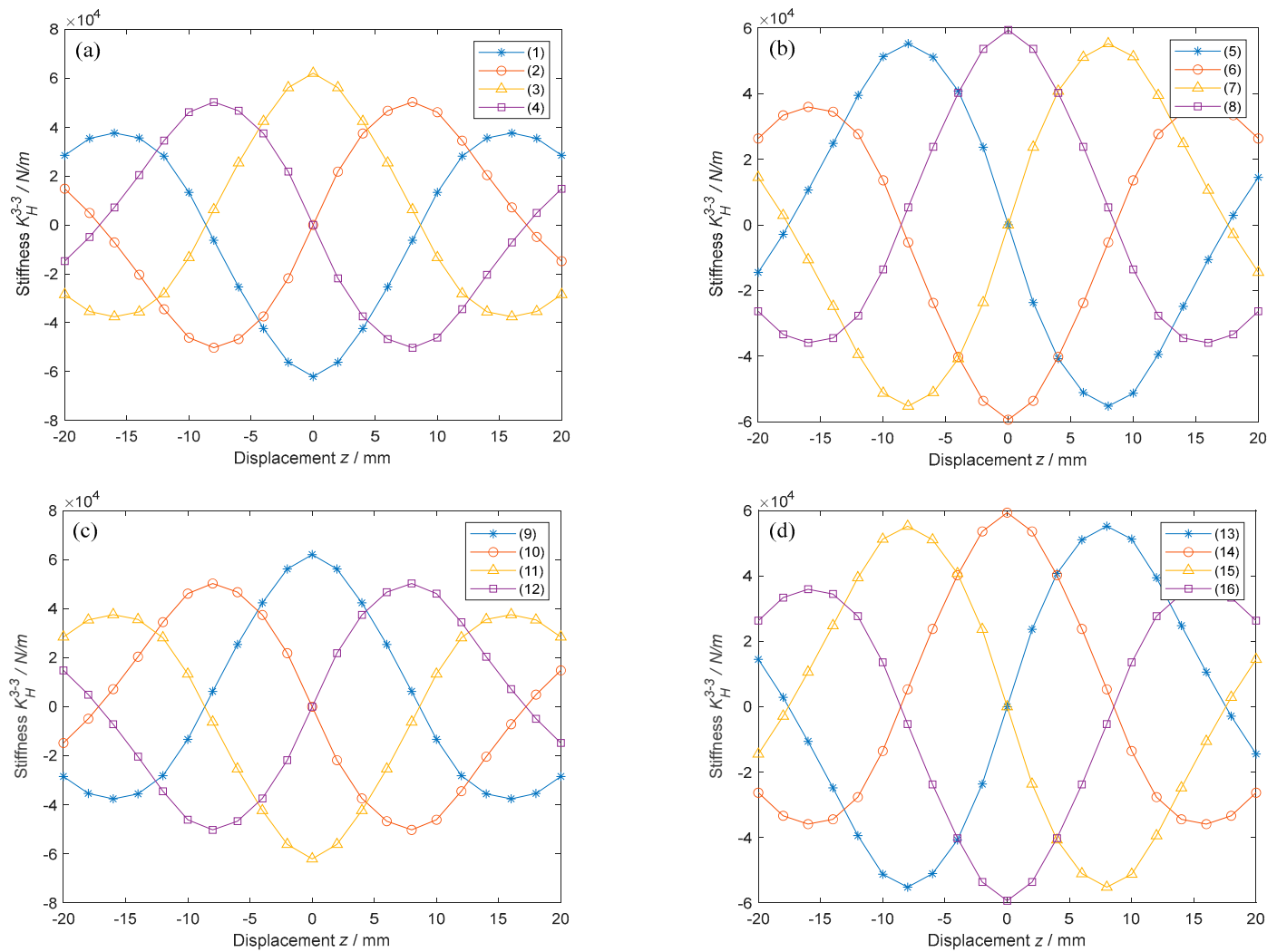


Figure 15. Stiffness curves of (a) 1st to 4th, (b) 5th to 8th, (c) 9th to 12th, and (d) 13th to 16th 3-3-type HCMSs.

5.5. A Case Study on Optimizing the Structure of the 3-3-Type HCMS

As shown above, the nonlinear negative stiffness characteristics of 3-3-type HCMSs are related to many geometric parameters. Generally speaking, it is complex to optimally design its structure due to the multi-variable optimization. In engineering applications, however, some geometric parameters can be determined in advance. Taking the 3-3-type HCMS in Figure 5 as an example, it can be seen that R_1 , R_4 are limited by the working space and d should be as small as possible in terms of installation. Once R_1 , R_4 , d are fixed, there are only two parameters to be optimized, namely R_2 and H . Here, we choose $R_1 = 10$ mm, $R_4 = 30$ mm, and $d = 2$ mm. Then, the stiffness curve at $z = 0$ with respect to R_2 and H is shown in Figure 16. The result shows that $R_2 = 14$ mm and $H = 11$ mm can be selected to obtain the maximum-amplitude negative stiffness.

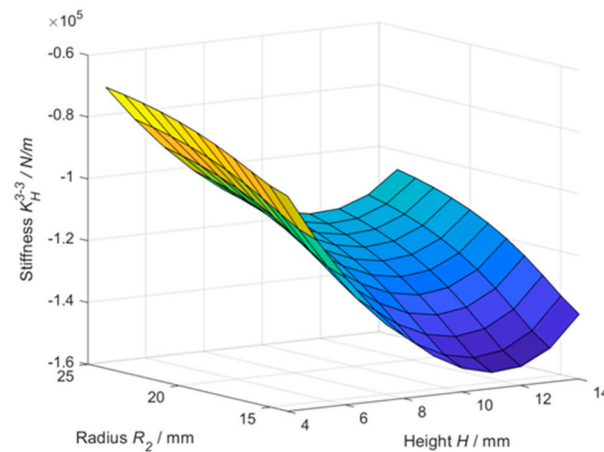


Figure 16. The stiffness surface with respect to R_2 and H ($z = 0$).

6. Potential Solution for HCMs with Larger-Amplitude and Wider-Range Negative Stiffness

In real-world applications, a larger-amplitude and wider-range negative stiffness is desirable. To address this challenge, the number of layers of the Halbach cylinder is increased to look for potential solutions. Here, the 5-3-type and 3-5-type HCMs are shown in Figure 17. As for these two HCMs, two cases are considered. The first one is that each magnetic ring in the outer and inner Halbach cylinders has the same height (i.e., 10 mm), which is denoted as Type I. The other one is that the total heights of the outer and inner Halbach cylinders are the same (i.e., 30 mm), which is denoted as Type II. Other geometric parameter values can be found in Table 4. Then, stiffness curves of the 5-3-type and 3-5-type HCMs are compared with that of the 3-3-type HCM, as shown in Figure 18. The results show that (i) under the same volume, increasing the layer number of either the outer Halbach cylinder or the inner Halbach cylinder cannot enlarge the amplitude and the displacement range of negative stiffness; (ii) by keeping the same height of magnetic rings, increasing the layer number of either the outer Halbach cylinder or the inner Halbach cylinder can enlarge the amplitude and the displacement range of negative stiffness; and (iii) the 5-3 Type II HCM is better than the 3-5 Type II HCM in terms of compact design and the amplitude of negative stiffness.

Despite the above promising characteristics, there are still the following disadvantages or limitations that deserve to be considered.

(1) Compared with traditional single-layer magnetic springs, more magnetic rings are utilized in the structure of HCMs. In this case, the total weight and volume of the magnetic spring will increase. At the same time, it needs to manufacture magnetic rings with different magnetization directions, leading to high costs.

(2) The performance of QZS is sensitive to its structural integrity, which will impose strict demands on manufacturing and assembling magnets. As for the HCM, there are multiple magnetic rings. Therefore, higher manufacturing and assembling precision is required. In return, the performance of the HCM is susceptible to manufacturing or assembling errors in practice.

(3) Both the design and the performance of HCMs depend strongly on the material properties of the magnets. In engineering applications, however, the possibility of demagnetization or even complete loss of magnetism may happen in magnets due to long-term service or severe working conditions.

(4) As for the HCM, there is a conflict between the amplitude and the uniformity of negative stiffness. The reason may be because only an inner Halbach cylinder is used.

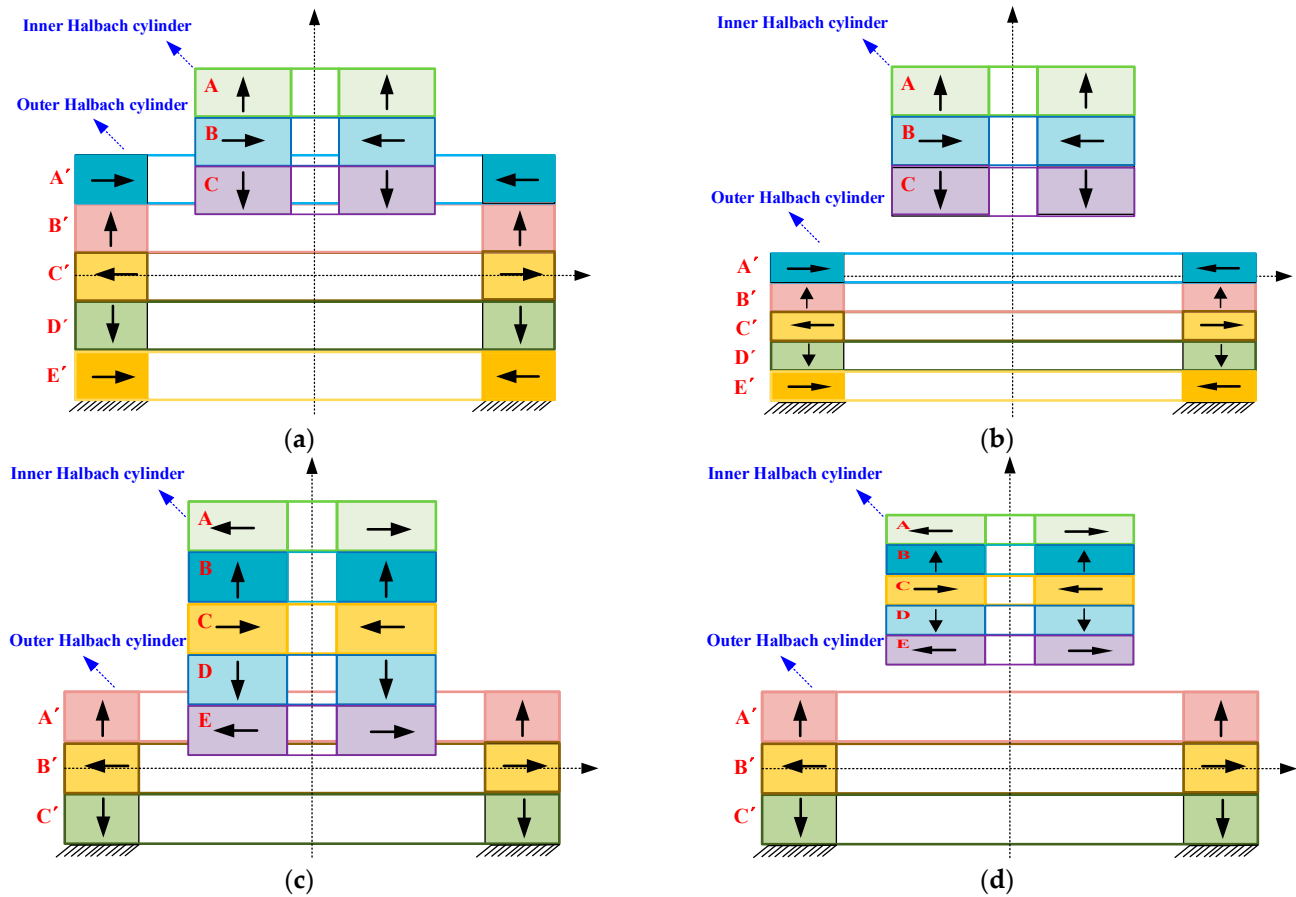


Figure 17. The structures of (a) 5-3 Type I (each magnetic ring has the same height); (b) 5-3 Type II (the outer and inner Halbach cylinders have the same height); (c) 3-5 Type I (each magnetic ring has the same height); and (d) 3-5 Type II (the outer and inner Halbach cylinders have the same height) HCMSs.

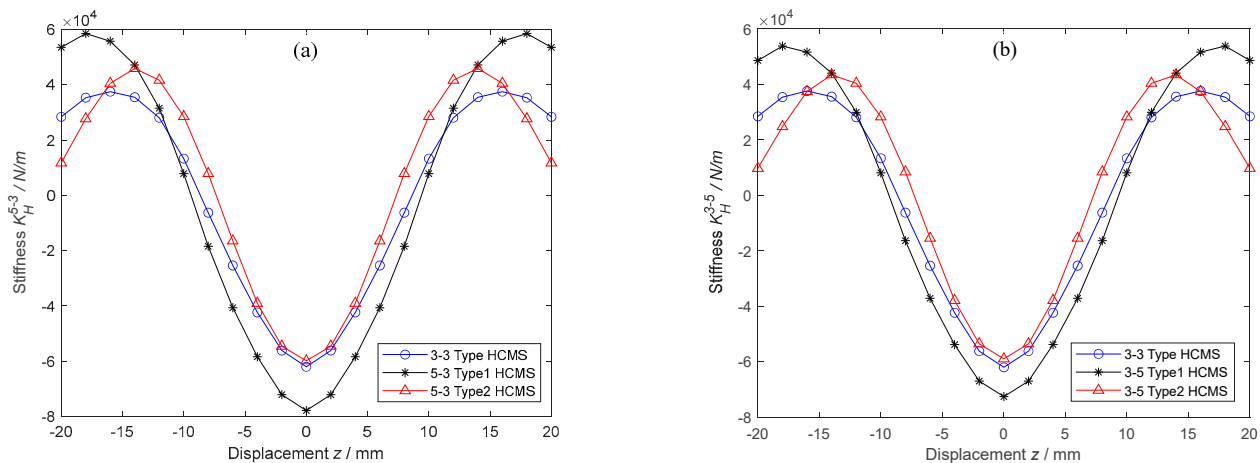


Figure 18. Stiffness curves of (a) 5-3-type and (b) 3-5-type HCMSs.

7. Conclusions

QZS is very promising for low-frequency vibration isolation due to the nonlinear HSLD stiffness, and a large-amplitude negative stiffness is needed for heavy-load applications. Thanks to the advantage of nocontact, magnetic springs have been widely utilized to obtain negative stiffness. However, the negative stiffness of existing magnetic springs is often not enough for heavy-load applications. To overcome this issue, this paper investigated novel magnetic springs with large-amplitude negative stiffness by introducing Halbach arrays.

The key outcome of this paper is to present a “building block” methodology for designing magnetic springs with specific requirements. Based on this, many variants of HCMSs can be easily analyzed and optimized. The main highlights of this paper include the following:

(1) The analytical stiffness formula of the HMCS is built based on the Amperian current model and the Biot–Savart law.

(2) HCMSs can generate negative stiffness with different equilibrium positions, and the amplitude of negative stiffness of HCMSs is much larger than that of existing single-layer magnetic springs.

(3) It is difficult to increase the amplitude and the uniformity of negative stiffness simultaneously, so a trade-off strategy is needed to design the HCMS.

(4) Increasing the layer number of Halbach cylinders can result in larger-amplitude and wider-range negative stiffness.

In future, novel HCMS configurations consisting of an outer cylinder and multiple inner cylinders can be investigated to deal with the conflict between the amplitude and the uniformity of negative stiffness. In addition, HCMS-integrated QZS will be designed and tested for heavy-load applications.

Author Contributions: Conceptualization, Z.C. and Y.X.; methodology, Z.C.; validation, Z.C., Y.Z. and A.W.; writing—original draft preparation, Z.C.; writing—review and editing, Y.X.; project administration, Z.C.; funding acquisition, Z.C. All authors have read and agreed to the published version of the manuscript.

Funding: This research was funded by the National Natural Science Foundation of China (grant number 52377204) and the Research Startup Fund Program for High-Level Talents of Shandong Xiehe University (grant number SDXHQD2025003).

Data Availability Statement: Data will be made available upon request to the corresponding author.

Acknowledgments: The authors thank all reviewers for their comments to improve this work.

Conflicts of Interest: The authors declare no conflicts of interest.

Abbreviations

The following abbreviations are used in this manuscript:

CMS	Circular magnetic spring
FEM	Finite element model
HCMS	Halbach-cylinder magnetic spring
HSLD	High static and low dynamic
QZS	Quasi-zero stiffness

References

1. Guruguntla, V.; Lal, M.; Ghantasala, G.S.P.; Vidyullatha, P.; Alqahtani, M.S.; Alsubaie, N.; Abbas, M.; Soufiene, B.O. Ride comfort and segmental vibration transmissibility analysis of an automobile passenger model under whole body vibration. *Sci. Rep.* **2023**, *13*, 11619. [[CrossRef](#)] [[PubMed](#)]
2. Okwudire, C.E.; Lee, J.Y. Minimization of the residual vibrations of ultra-precision manufacturing machines via optimal placement of vibration isolators. *Precis. Eng.* **2013**, *37*, 425–432. [[CrossRef](#)]
3. Maneerat, P.; Rungskunroch, P. Impact of earthquakes on California’s Railways: A comprehensive correlation analysis of magnitude and hypocenter depths with infrastructure accident. *Transp. Res. Interdisc.* **2024**, *24*, 101082. [[CrossRef](#)]
4. Wang, Z.; Fan, K.Q.; Zhao, S.Z.; Wu, S.X.; Zhang, X.; Zhai, K.J.; Li, Z.Q.; He, H. Archery-inspired catapult mechanism with controllable energy release for efficient ultralow-frequency energy harvesting. *Appl. Energy* **2024**, *356*, 122400. [[CrossRef](#)]
5. Alabuzhev, P.M. *Vibration Protection and Measuring Systems with Quasi-Zero Stiffness*; CRC Press: Boca Raton, FL, USA, 1989.
6. Yan, G.; Zou, H.X.; Wang, S. Large stroke quasi-zero stiffness vibration isolator using three-link mechanism. *J. Sound Vib.* **2020**, *478*, 115344. [[CrossRef](#)]

7. Gatti, G.; Shaw, A.D.; Goncalves, P.J.P. On the detailed design of a quasi-zero stiffness device to assist in the realisation of a translational Lanchester damper. *Mech. Syst. Signal Process.* **2020**, *164*, 108258. [\[CrossRef\]](#)
8. Carrella, A.; Brennan, M.J.; Kovacic, I. On the force transmissibility of a vibration isolator with quasi-zero-stiffness. *J. Sound Vib.* **2009**, *322*, 707–717. [\[CrossRef\]](#)
9. Liu, C.; Yu, K. Superharmonic resonance of the quasi-zero-stiffness vibration isolator and its effect on the isolation performance. *Nonlinear Dyn.* **2020**, *100*, 95–117. [\[CrossRef\]](#)
10. Liu, X.; Huang, X.; Hua, H. On the characteristics of a quasi-zero stiffness isolator using Euler buckled beam as negative stiffness corrector. *J. Sound Vib.* **2013**, *332*, 3359–3376. [\[CrossRef\]](#)
11. Li, M.; Cheng, W.; Xie, R. A quasi-zero-stiffness vibration isolator using a cam mechanism with user-defined profile. *Int. J. Mech. Sci.* **2021**, *189*, 1059. [\[CrossRef\]](#)
12. Chen, Z.S.; Chen, Z.W.; Nie, G.F.; Li, K.Q. Analytical and experimental investigations on low-frequency simultaneous vibration isolation and energy harvesting using magnetic rings. *IEEE Access* **2024**, *12*, 32668–32678. [\[CrossRef\]](#)
13. Zhu, Q.B.; Chai, K. Magnetic negative stiffness devices for vibration isolation systems: A state-of-the-art review from theoretical models to engineering applications. *Appl. Sci.* **2024**, *14*, 4698. [\[CrossRef\]](#)
14. Wu, J.L.; Zeng, L.Z.; Han, B.; Zhou, Y.F.; Luo, X.; Li, X.Q.; Chen, X.D.; Jiang, W. Analysis and design of a novel arrayed magnetic spring with high negative stiffness for low-frequency vibration isolation. *Int. J. Mech. Sci.* **2022**, *216*, 106980. [\[CrossRef\]](#)
15. Li, B.L.; Wang, W.; Li, Z.L.; Wei, R.H. Hand-held rolling magnetic-spring energy harvester: Design, analysis, and experimental verification. *Energy Convers. Manag.* **2024**, *301*, 118022. [\[CrossRef\]](#)
16. Akoun, G.; Yonnet, J.P. 3D Analytical calculation of the forces exerted between two cuboidal magnets. *IEEE Trans. Magn.* **1984**, *20*, 1962–1964. [\[CrossRef\]](#)
17. Zheng, Y.S.; Zhang, X.N.; Luo, Y.J.; Yan, B.; Ma, C.C. Design and experiment of a high-static-low-dynamic stiffness isolator using a negative stiffness magnetic spring. *J. Sound Vib.* **2016**, *360*, 31–52. [\[CrossRef\]](#)
18. Yu, N.; Fei, X.Y.; Sun, H.; Wu, Z.M.; Yan, B. Rhombus-type magnetic-levitation structure for low-frequency vibration isolation. *Mech. Syst. Signal Process.* **2025**, *225*, 112289. [\[CrossRef\]](#)
19. Zhou, J.X.; Wang, K.; Xu, D.L.; Ouyang, H.J.; Fu, Y.M. Vibration isolation in neonatal transport by using a quasi-zero-stiffness isolator. *J. Vib. Control* **2018**, *24*, 3278–3291. [\[CrossRef\]](#)
20. Chen, Z.W.; Chen, Z.S.; Wei, Y.X. Quasi-zero stiffness-based synchronous vibration isolation and energy harvesting: A comprehensive review. *Energies* **2022**, *15*, 7066. [\[CrossRef\]](#)
21. Leng, D.X.; Zhu, Z.H.; Xu, K.; Li, Y.C.; Liu, G.J. Vibration control of jacket offshore platform through magnetorheological elastomer (MRE) based isolation system. *Appl. Ocean Res.* **2021**, *114*, 102779. [\[CrossRef\]](#)
22. Halbach, K. Design of permanent multipole magnets with oriented rare earth cobalt material. *Nucl. Instrum. Methods Phys. Res.* **1980**, *169*, 1–10. [\[CrossRef\]](#)
23. Halbach, K. Applications of permanent magnets in accelerators and electron storage rings. *J. Appl. Phys.* **1985**, *57*, 3605–3608. [\[CrossRef\]](#)
24. Lee, M.G.; Lee, S.Q.; Gweon, D.G. Analysis of Halbach magnet array and its application to linear motor. *Mechatronics* **2004**, *14*, 115–128. [\[CrossRef\]](#)
25. Chen, Z.S.; Chen, Z.W.; Wei, Y.X.; Xiong, Y.P. Nonlinear electromagnetic vibration energy harvester comprising dual helical-plane springs and multiple Halbach arrays for low-frequency and small-amplitude vibrations. *Energy Rep.* **2024**, *11*, 1363–1375. [\[CrossRef\]](#)
26. Maamer, B.; Tounsi, F.; Kaziz, S.; Jaziri, N.; Boughamoura, A. A Halbach cylinder-based system for energy harvesting from rotational motion with high power density. *Sensor Actuat. A-phys.* **2022**, *337*, 113428. [\[CrossRef\]](#)
27. Sim, M.S.; Ro, J.S. Semi-analytical modeling and analysis of Halbach array. *Energies* **2020**, *13*, 1252. [\[CrossRef\]](#)
28. Oliveira, M.H.; Miranda, J.A. Biot-Savart-like law in electrostatics. *Eur. J. Phys.* **2001**, *22*, 31. [\[CrossRef\]](#)

Disclaimer/Publisher’s Note: The statements, opinions and data contained in all publications are solely those of the individual author(s) and contributor(s) and not of MDPI and/or the editor(s). MDPI and/or the editor(s) disclaim responsibility for any injury to people or property resulting from any ideas, methods, instructions or products referred to in the content.